Review of Scientific Instruments

RESEARCH ARTICLE | APRIL 03 2023

Focused laser differential interferometry post-processing methodology for flowfields with circular symmetry

Giannino Ponchio Camillo ; Alexander Wagner

Rev Sci Instrum 94, 045102 (2023)
https://doi.org/10.1063/5.0132874

Articles You May Be Interested In

Measurement of hypersonic turbulent boundary layer on a flat plate using cylindrical focused laser differential interferometer

Physics of Fluids (March 2023)

Polynomial ridge flowfield estimation

Physics of Fluids (December 2021)

AIP Publishing

Review of Scientific Instruments ARTICLE scitation.org/journal/rsi

Focused laser differential interferometry post-processing methodology for flowfields with circular symmetry

Cite as: Rev. Sci. Instrum. 94, 045102 (2023); doi: 10.1063/5.0132874
Submitted: 31 October 2022 • Accepted: 13 March 2023 •
Published Online: 3 April 2023

View Online Export Citation CrossMark

Giannino Ponchio Camillo[a] and Alexander Wagner[b]

AFFILIATIONS

German Aerospace Center (DLR), Institute of Aerodynamics and Flow Technology, Göttingen, Germany

[a]Author to whom correspondence should be addressed: Giannino.PonchioCamillo@dlr.de
[b]**Electronic mail:** Alexander.Wagner@dlr.de

ABSTRACT

An analytic methodology is presented to reconstruct the pressure waveform of flowfields with circular symmetry from the phase shift detected with Focused Laser Differential Interferometry (FLDI). A weak blast wave generated by an electric spark in ambient air is investigated with the proposed approach. Values of separation distance between the differentiating foci of the FLDI Δx of 76, 120, 175, and 252 μm are employed to probe the flowfield at locations between 3 and 50 mm from the spark source. In a subset of these distances, reference measurements of peak pressure obtained with a surface pressure sensor indicate good agreement with the reconstructed data when small separation distances are used. Further analysis of FLDI reconstructed data is conducted using theoretical correlations for N-waves in terms of the distribution of pressure peak amplitude and compression phase as the wave front propagates. Agreement with theory is verified for all differentiation separation distances except the largest, for which peak pressure comparison shows a 10% loss of measured vs predicted value. A computational FLDI is employed to scrutinize the simplifying hypotheses supporting the waveform reconstruction approach. The direct comparison between experimental and computational FLDI output reveals additional discrepancies for intermediate Δx values but very good agreement for the smallest Δx. The proposed methodology is thus verified to be reasonable, upon appropriate minimization of the FLDI differentiation distance. A parametric analysis using computational FLDI indicates the adequate value of FLDI Δx to be 20% or less of the flowfield characteristic length in terms of density gradient.

I. INTRODUCTION

Focused Laser Differential Interferometry (FLDI) is a non-invasive measurement technique that measures flowfield density fluctuations. Its distinct spatial and temporal resolutions render it especially suited for ground-based experimental investigation of hypersonic flowfields. Attention to this technique has been growing steadily within the community since Refs. 1 and 2. This is evidenced by the increasing number of laboratories implementing the FLDI technique in recent years.[3–8]

Owing to the broad bandwidth of the FLDI and its robustness to external noise, the evaluation of the frequency spectrum of FLDI data using only simplified post-processing approaches has been proven to already offer valuable information about the probed flowfields.[9–13] Nonetheless, a rigorous conversion of FLDI data into flowfield quantities such as density fluctuation is required in order to fully explore the capabilities of the technique and allow quantitative evaluations. However, this task is made difficult by some of the key features of the FLDI. The ability of the FLDI to dampen frequencies away from its focus and the finite differentiation it performs must be considered when attempting to convert the FLDI output back into flowfield variables.

The extraction of quantitative density data while respecting the complexity of the FLDI response has been explored by means of transfer function analysis.[2,14] This methodology has been initially shown for special types of flowfields such as uniformly distributed turbulence or Gaussian jets.[2] Agreement between pitot-based pressure fluctuations and FLDI data processed with transfer functions has also been experimentally demonstrated in a Mach 6 free stream.[15] Recent efforts have included the deduction of transfer functions for more complex flowfields, encompassing two and three-dimensional sinusoidal disturbances, either infinitesimally thin, uniform within a finite volume, or modulated by a Gaussian intensity profile.[16,17] A sensitivity function for the FLDI has been developed using transfer functions and verified using a turbulent air jet[18,19] and wind-tunnel disturbances.[20] A solution for the inverse FLDI problem for single-direction, continuous-frequency waves has been proposed and experimentally verified against supersonic free stream pitot data.[21]

These efforts represent significant advancements toward a better understanding of the FLDI technique and the proper treatment of the data it offers. Nonetheless, at each instant in time, the FLDI output from a three-dimensional density field consists of a single scalar value as a result of successive integrals and differences of flowfield quantities. Therefore, assumptions about the topology of the flowfield are inevitable when trying to reverse this problem.[22] The flowfield models recently explored in Refs. 16–22 are able to represent many practical applications, such as turbulent jets, free stream turbulence, and acoustic radiation, among others. Still, they must be adjusted according to the flowfield at hand and might not offer the easiest solution for all kinds of flowfields. Furthermore, if the flowfield model must be adjusted manually in a case-by-case fashion, it is important to have a way to independently verify the obtained results.

One such way is to numerically simulate the FLDI response using a ray-tracing scheme,[23] which is able to reproduce how the flowfield variations are perceived by the FLDI beams. This computational FLDI (cFLDI) has been shown to produce accurate quantitative results against experiments for a static laminar jet[24] and a complex shock-dominated dynamic flowfield.[25] The cFLDI has since been employed to further study the technique. For example, the dependence between the FLDI sensitivity length and the beam divergence angle has been verified using parametric analysis.[26] The ability of the FLDI instrument to see through unwanted signals at the edges of the probing volume, such as the wall boundary layers or the nozzle shear layer in hypersonic wind-tunnels, has also been explored.[27] Furthermore, cFLDI simulated on the DNS solution of a wind-tunnel boundary layer has been investigated as a means to inform constraints for the FLDI application.[28]

This type of insight is allowed by the proven physical fidelity of the cFLDI, which, therefore, places it as a tool to explore methodologies that aim at obtaining quantitative information from FLDI data but are only feasible by assuming model parameters or adopting certain simplifying hypotheses. Once the flowfield is reconstructed from real FLDI measurements, a simulated FLDI response may be obtained with the high-fidelity ray-tracing algorithm; then, a comparison between the real and simulated FLDI data allows for assessing the validity of any assumptions or simplifications involved in the post-processing method.

The goal of the present work is to contribute toward the inclusion of circularly symmetric flowfields in the subset of special cases for which FLDI data can be fully regressed into flowfield quantities through analytic approaches. A number of assumptions will be necessary to reach this objective. In light of the physical accuracy of cFLDI demonstrated in Refs. 24 and 25, simulations using an implementation of the FLDI ray-tracing algorithm are employed to support the analysis of the results obtained with the analytic approach.

The object of study to apply and analyze the proposed methodology is a weak blast wave generated by an electric spark in ambient air at rest, using a setup detailed in a previous study by the present authors.[8] The study of blast waves pertains to various applications ranging from explosive detonations to sonic booms.[29,30] A review of the diagnostic tools currently available for the experimental study of such flows is summarized in Ref. 31. In that work, laser interferometry was suggested as a solution to overcome the bandwidth and sensitivity limitations of consolidated techniques such as dynamic pressure transducers and condenser microphones. The FLDI presents similar capabilities with further advantages such as adjustable sensitivity and simplicity, and may, therefore, be of interest to related investigations.

The contents of this paper are summarized as follows: Experimental measurements of a weak spark-generated blast wave are collected using FLDI at multiple distances from the spark source. A methodology is presented to obtain the spherical distribution of quantitative acoustic pressure from such measurements, following a series of simplifying assumptions. No other instruments of similar capability were available to produce detailed reference measurements for comparison with the FLDI data. Therefore, the obtained results are verified using multiple complementary approaches. In a first step, peak pressures are compared to direct measurements using a fast piezoelectric pressure transducer, performed at locations allowed by the geometric constraints of the experimental setup. Next, the obtained waveforms are compared with analytic correlations involving compression phase duration and peak pressure for propagating acoustic pulses. Finally, the FLDI response to the reconstructed flowfield is simulated with the ray-tracing scheme and compared to the original experimental data. The simplifying assumptions necessary for the flowfield reconstruction methodology are analyzed in light of observed discrepancies to help identify eventual constraining parameters that control the fidelity of the reconstruction. The emphasis is given to a single location along the blast wave trajectory, namely, 30 mm from the spark, although the procedure is applicable to any given location.

II. THEORETICAL BACKGROUND

A. Blast waves

A blast wave in a fluid at rest can be originated by a localized instantaneous release of energy. The change in local pressure and temperature propagates away from the origin of the event at the speed of sound in the immediate medium. Because the speed of sound is larger in regions with higher temperatures, those portions of the disturbance propagate faster than those in their vicinity. A discontinuity is hence formed as a shock wave front,[29] which propagates supersonically with respect to the undisturbed fluid.

In the case of radially propagating blast waves, the strength of the shock wave front will progressively become weaker due to volume divergence, dissipation, and molecular relaxation. Eventually, the blast wave becomes so weak that it propagates approximately at the sound speed of the non-disturbed gas, becoming an acoustic wave. This process is accompanied by changes in the pressure signature, best described in terms of acoustic pressure, i.e., the overpressure with respect to the undisturbed field. The blast wave is marked by a sharp and narrow compression phase (positive acoustic pressure), followed by a longer and smoother expansion phase (negative acoustic pressure). As the blast wave propagates, the amplitude of the positive phase decreases and the trailing edge of the negative phase becomes sharper due to the slightly higher local sound speed. The pressure waveform then describes a so-called N-wave.

Close to the blast wave source, the spark-generated blast wave is best approximated as a cylindrical shock due to the finite length of the spark. In the acoustic limit region, which is evaluated in more detail here, the distance to the cylindrical source is an order of magnitude higher than the length of the spark. In such a case, the flowfield generated by a point-source is a better representation of the local blast wave disturbance than the one generated by an infinite line. Therefore, a point-source hypothesis is considered in this work.

For the spherical propagation of N-waves, Ref. 32 presented analytic expressions from the linear theory of sound in gases (weak-shock theory) amenable to experimental comparisons, having also approximated an electric spark as a point-source downstream of a few spark lengths from the discharge. The methodology presented therein consisted of calculating the acoustic pressure peaks behind the shock, P, expected from theory, given measurements of compression phase duration, T, over several distances from the N-wave source. In the present work, both peak pressure and compression phase duration will be obtained directly from FLDI measurements. The cited methodology will, therefore, be employed to verify whether the obtained (T, P) pairs are physically consistent with the expected behavior of an N-wave.

The equations and procedures from Ref. 32 pertinent to the present work are briefly reproduced next. A different variable notation than presented in that work is used here for clarity. The compression phase duration T of the N-wave when the spherical wave front has propagated through a distance R from its origin can be written in terms of its value at an arbitrary reference propagation distance (subscript 0) as

$$T = T_0\sqrt{1 + \sigma_0 \,\ln\left(R/R_0\right)}. \tag{1}$$

The non-dimensional parameter σ_0 in this equation is a function of the N-wave compression phase duration and peak acoustic pressure at the reference distance, as well as the undisturbed medium pressure P_{amb}, sound speed c_{amb}, and specific heat ratio γ as

$$\sigma_0 = (\gamma + 1)R_0 P_0/(2\,\gamma\, P_{\mathrm{amb}}\, c_{\mathrm{amb}}\, T_0). \tag{2}$$

It is noted in Ref. 32 that through Eq. (1), T^2 as a function of $\log R$ describes a straight line with slope equal to $\sigma_0 T_0^2 \ln 10$. This slope may be obtained from a dataset of measured compression phases T at multiple locations R. Since the reference location (subscript 0) is arbitrary, the slope evaluates σ for any T. Finally, Eq. (2) defines the peak pressure P from weak-shock theory, which corresponds to the experimentally measured T.

B. Focused laser differential interferometry

Laser interferometry is achieved by combining two coherent monochromatic beams presenting equal intensity and linear polarization in the same direction, after having traveled through different optical paths. The interference resulting from their superposition causes the combined light intensity to be modulated by any difference in phase between the beams. This difference in phase is accumulated along the entirety of the paths described by the beams. The intensity of the recombined beam is detected as a scalar value, resulting from integrating the light intensity changes across the face of the beam at the detector. A differential interferometer is obtained when the beams go through the same medium, separated by a small distance.

In the special case of a focused laser differential interferometer (FLDI), the two beams are focused to a point within the probed volume. These two defining characteristics are responsible for making the sensitive volume of the FLDI dependent on the wavelength of the disturbances in the probed flowfield, with high-frequency content being rejected away from the focal plane. If the wavelength of the flowfield fluctuation in a certain portion of the beams is too small relative to their cross-section size, the contribution of those disturbances to the final signal is averaged out through integration at the face of the detector. For a thorough discussion about this, see Ref. 2.

For the reconstruction of spherical blast waves from FLDI detection presented in this work, a simplified approach that disregards the FLDI wavelength-dependent sensitivity is adopted. The validity of this assumption is verified with the assistance of a computational model that fully represents the real apparatus. This is made possible by observing that the series of processes involved in the interaction between the probed flowfield and the FLDI beams is challenging to reverse but straightforward to reproduce. Simplifying hypotheses can, therefore, be evaluated by comparing the high-fidelity simulated FLDI output of the reconstructed field with the experimental FLDI data that originated it.

The computational FLDI used in this work is based on the ray-tracing model of Ref. 23 and is similar in terms of implementation and application to the recent validation work of Ref. 25. A summary of the pertinent concepts and equations used in this work is given next.

A Cartesian coordinate system is defined with the z axis parallel to the optical axis (direction of propagation of the beams), the x axis parallel to the direction of separation between the beams, and the origin at the midpoint between the FLDI foci. Each beam is discretized into a finite number of rays, parameterized in a convenient auxiliary coordinate system to account for the focusing of the beams in a computationally effective manner. The FLDI used in this work presents a Gaussian, circular beam cross-section. Therefore, a polar coordinate system $(\tilde{r}, \theta)$ is used to distribute the rays around a center point in the cross-section with $0 \leq \theta < 2\pi$ and $0 < \tilde{r} \leq \tilde{r}_{max}$. The radial coordinate $\tilde{r}$ is non-dimensionalized with respect to the local Gaussian beam radius $w(z)$,

$$w(z) = \sqrt{w_0^2\left(1 + \left[\frac{\lambda_0 z}{\pi w_0^2}\right]^2\right)}, \tag{3}$$

where λ_0 is the light wavelength and $w_0 = \lambda_0/\pi\theta_d$ is the waist of the beam at the focal plane $(z = 0)$, with θ_d the beam divergence angle. An upper limit for the non-dimensional radial coordinate of $\tilde{r}_{max} = 2$ (two times the local Gaussian beam radius, in dimensional coordinates) is adopted.[23]

A greatly simplified exemplary computational mesh is illustrated in the Cartesian space in Fig. 1. For clarity, only a region very

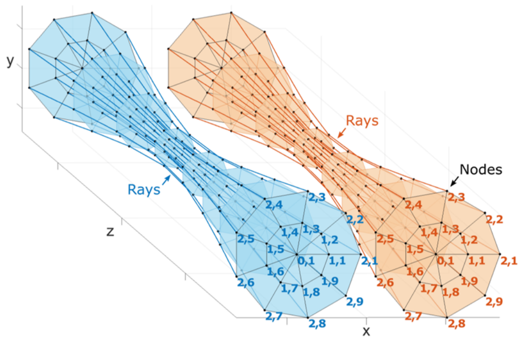

FIG. 1. Illustrative cFLDI mesh, very coarse for clarity. A pair of beams of an FLDI very near its center plane are shown in different colors, each denoting one plane of orthogonal polarization. Lines connecting the nodes of individual rays are marked. The labels of nodes on the front plane are numbered as coordinate pairs: radial coordinate and angle coordinate.

close to the focus of the system is shown. The pair of orthogonally polarized beams is displayed in different colors. The spatial discretization is performed through the definition of nodes as the $(\tilde{r}, \theta)$ pairs at each z-plane and rays connecting all nodes with the same non-dimensional coordinates across all z-planes. The discretization of each beam is identical except for an offset in the x direction.

The rays shown in Fig. 1 are treated as pairs to perform the differential operations. Each ray in one of the beams has a correspondent counterpart in the other, as labeled on the front plane of the figure. Flowfield density values are interpolated to the FLDI nodes at each instant in time. The total number of z planes is even, so that all rays undergo a quadrant inversion in θ as they cross $z = 0$ to account for image inversion through the focus.[25] This is performed internally in the algorithm and is not shown in Fig. 1.

Fluctuations in density ρ in the flowfield crossing the rays shown in Fig. 1 cause their optical paths to vary due to changes in the local refraction index n. A difference in the optical paths traveled by two monochromatic and coherent light rays causes a difference in phase $\Delta\phi$ between them.[33] These effects are combined as

$$\Delta\phi = \frac{2\pi K}{\lambda_0}\left(\int_{C_1}\rho(s_1)\,ds_1 - \int_{C_2}\rho(s_2)\,ds_2\right), \tag{4}$$

with K the Gladstone–Dale constant for the light wavelength λ_0, C_1 and C_2 defining the spatial path traveled by each beam, and the field density parameterized as $\rho(s_i)$, with s_i the spatial variable that describes C_i.

Equation (4) is valid for each corresponding pair of light rays that compose the two beams of one FLDI. Upon recombination and projection of the two beams back to a common polarization plane, the resulting light intensity of each ray is modulated by the phase difference $\Delta\phi$ as[33]

$$I = I_1 + I_2 + 2\sqrt{I_1 I_2}\,\cos\Delta\phi, \tag{5}$$

where I_1 and I_2 are the intensities of the separate rays, and I is the intensity of the recombined ray.

The output of the FLDI is given by the average of the intensities of all rays, weighted according to the intensity profile of the beam. For a Gaussian beam, the normalized intensity profile is described by $\tilde{I}_0(\tilde{r}) = 2\pi^{-1}\exp(-2\tilde{r}^2)$. If the undisturbed orthogonally polarized pair is adjusted to present an initial phase difference of $\pi/2$ and an equal intensity distribution $\tilde{I}_0/2$, the normalized intensity at the face of the detector D becomes,

$$\tilde{I}_D = \iint_D \left(\tilde{I}_0(\tilde{r},\theta) + \tilde{I}_0(\tilde{r},\theta)\,\sin\Delta\phi(\tilde{r},\theta)\right) d\tilde{r}\,d\theta, \tag{6}$$

with $\Delta\phi(\tilde{r},\theta)$ evaluated using Eq. (4) for each ray. Experimental FLDI data are usually given in terms of an equivalent phase shift $\Delta\Phi$ that represents the normalized intensity $\tilde{I}_D$ of Eq. (6). With the light intensity normalization chosen such that the integral of $\tilde{I}_0$ over D is unity, the equivalent phase shift $\Delta\Phi$ becomes

$$\Delta\Phi = \sin^{-1}\left(\iint_D \tilde{I}_0(\tilde{r},\theta)\,\sin\Delta\phi(\tilde{r},\theta)\,d\tilde{r}\,d\theta\right). \tag{7}$$

In the present work, all integrals are numerically calculated using trapezoidal integration. Equations (4) and (7), when used with an appropriate computational mesh, fully represent the FLDI probing a given flowfield. The cFLDI mesh is kept fixed in space, which implies ignoring any steering of the rays caused by local gradients of refraction index. Nonetheless, the effect of this simplification on the accuracy of cFLDI simulations is negligible. This has been confirmed in Ref. 25, in which a complex experimental shock-dominated flowfield was accurately represented by cFLDI simulation using that same constraint.

It is noteworthy that, when performing cFLDI simulations, the operation of interpolating flowfield data to FLDI nodes presents a marked influence on computational cost. For the analysis of a spherically symmetrical disturbance such as the spark-generated blast wave of the present work, the magnitude of the field disturbance at any location is simply described in terms of the radial variable r of a spherical coordinate system. By shifting the origin of the FLDI Cartesian system to coincide with the source of the disturbance, the coordinates of each FLDI node (x_i, y_i, z_i) are simply represented in that system as $r_i = \sqrt{x_i^2 + y_i^2 + z_i^2}$. This way, the density value at each node is efficiently interpolated from the field disturbance data.

C. Reconstruction of spherical waveforms from FLDI data

Figure 2 illustrates the principle of the flowfield investigation in this work. The generated disturbance flowfield is approximated as spherical, such that at any given instant it is fully described by the spherical coordinate r, with origin coincident with the location of the disturbance source. The interferometric pair of the FLDI is parallel to the Cartesian z and crosses x at a distance x_0 to the disturbance source. The separation distance between the orthogonally polarized beams is Δx. In this section, a methodology to obtain the radial distribution of acoustic pressure based on measured FLDI data is presented.

The problem of interpreting data from spherically diverging acoustic N-waves using experimental techniques that probe along straight lines was addressed in detail in Refs. 31 and 34. A similar procedure will be adopted here, with a few additional assumptions

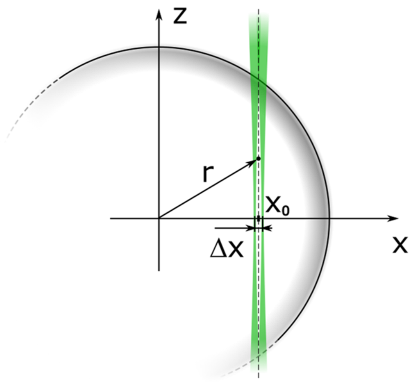

FIG. 2. Schematic of one FLDI bundle (green) probing a circular disturbance (gray). Relevant Cartesian and spherical coordinates are shown. Dimensions not to scale.

and considerations specific to the FLDI. Simplifying hypotheses are adopted and critically evaluated later in this work with the support of experiments and computational FLDI.

First, the line integrals in Eq. (4) are expressed in spherical coordinates. The FLDI coordinate system is defined such that the center lines of the paths C_1 and C_2 are parallel to the Cartesian z axis. The volume described by the FLDI beams is assumed to be slender enough that the problem can be simplified to the two dimensions shown in Fig. 2 and that the small divergence angle of the beams can be neglected within the reconstruction method.

It is noteworthy that with these assumptions, the method described here is applicable in cases of circular symmetry around a point, such as a sphere, and also around an axis, such as a cone or a cylinder with the probing direction perpendicular to their center axis. The integration paths s_i in Eq. (4) are hence defined by a constant x, i.e., $s_i = s_i(x_i, z)$ and $ds_i = dz$. A line of constant $x = x_i$ is written in spherical coordinates as $r = \sqrt{x_i^2 + z^2}$, yielding $dz = r\,dr/\sqrt{r^2 - x_i^2}$. Finally, considering that the disturbance field is symmetric around $z = 0$ and that $r_i|_{z=0} = x_i$ and $r_i|_{z=\infty} = \infty$, each integral in Eq. (4) becomes

$$\int_{-\infty}^{\infty} \rho(x_i, z)\, dz = 2\int_{x_i}^{\infty} \frac{\rho(r)\, r}{\sqrt{r^2 - x_i^2}}\, dr. \tag{8}$$

This integral is now analyzed in light of the problem at hand. The flowfield surrounding the blast wave is assumed to be initially at rest. Hence, although the upper limit of the integral in Eq. (8) is infinite, the integration length of practical significance will be defined by the blast wave radius. Furthermore, except for very close to the origin of the blast wave, the acoustic disturbance defined by it will be largely concentrated in the inner vicinity of its radius at any instant in time, and zero everywhere else. With these two observations, it is reasonable to consider $z \ll x_i$ within the relevant integration length in Eq. (8). Finally, for a small displacement Δx, consequently, $x + \Delta x \approx x$, $\Delta r \approx \Delta x$, and $r + \Delta r \approx r$. By defining the location of each FLDI beam as $x_i = x_0 \pm \Delta x/2$ (see Fig. 2), Eq. (8) can be approximated for each beam as

$$\begin{aligned}\int_{x_0 - \frac{\Delta x}{2}}^{\infty} \frac{\rho(r)\, r}{\sqrt{r^2 - \left(x_0 - \frac{\Delta x}{2}\right)^2}}\, dr &\approx \int_{x_0}^{\infty} \frac{\rho\left(r - \frac{\Delta r}{2}\right) r}{\sqrt{r^2 - x_0^2}}\, dr, \\ \int_{x_0 + \frac{\Delta x}{2}}^{\infty} \frac{\rho(r)\, r}{\sqrt{r^2 - \left(x_0 + \frac{\Delta x}{2}\right)^2}}\, dr &\approx \int_{x_0}^{\infty} \frac{\rho\left(r + \frac{\Delta r}{2}\right) r}{\sqrt{r^2 - x_0^2}}\, dr.\end{aligned} \tag{9}$$

With the integrals now having the same integration limits, Eq. (4) is rewritten as

$$\Delta\phi = \frac{2\pi K}{\lambda_0}\left[2\int_{x_0}^{\infty}\left(\rho\left(r - \frac{\Delta r}{2}\right) - \rho\left(r + \frac{\Delta r}{2}\right)\right)\frac{r}{\sqrt{r^2 - x_0^2}}\, dr\right]. \tag{10}$$

It is possible to isolate the density difference in the integrand of Eq. (10) by means of an Abel transform, following Refs. 31 and 34,

$$F(x) = 2\int_x^{\infty} \frac{f(r)\, r}{\sqrt{r^2 - x^2}}\, dr, \tag{(11a)}$$

$$f(r) = -\frac{1}{\pi}\int_r^{\infty} \frac{dF(x)}{dx}\frac{dx}{\sqrt{x^2 - r^2}}. \tag{(11b)}$$

An expression describing the radial distribution of density differences as a function of phase differences measured along a secant line is thus obtained,

$$\rho\left(r - \frac{\Delta r}{2}\right) - \rho\left(r + \frac{\Delta r}{2}\right) = -\frac{\lambda_0}{2\pi^2 K}\int_r^{\infty} \frac{d\Delta\phi(x)}{dx}\frac{dx}{\sqrt{x^2 - r^2}}. \tag{12}$$

Note that Eq. (12) requires knowledge of the spatial distribution of phase differences. However, the FLDI system outputs a time-resolved phase difference at a fixed spatial location, namely the optical axis of the FLDI system. This can be addressed by assuming that the waveform probed by the FLDI travels with a uniform velocity. Indeed, the weak spark-generated blast wave analyzed here is produced with the same experimental setup as in Ref. 8, in which it was verified to present little variation from $M = 1$ as close as 20 mm from its source. Furthermore, the hypothesis of uniform propagation velocity was tested in Ref. 31 by means of numerically simulating blast wave convection using the generalized Burger's partial differential equation. Terms accounting for non-linearity, dissipation, and relaxation processes were included, and the results revealed maximum errors close to 1% for the estimates of peak pressure and positive phase duration.

Through this assumption, a time-resolved $\Delta\phi(t)$ is converted into a spatially-resolved $\Delta\phi(x)$ by using

$$x = x_0 - (t - t_0)c_0, \tag{13}$$

where c_0 is the convection velocity and t_0 is the time corresponding to a reference coordinate x_0, which may be conveniently defined without loss of generality.

With the radial distribution of differences in density obtained from Eq. (12), an estimate of field amplitudes is obtained as follows. Assuming that the density field is composed of small disturbances, the local density can be expressed as the sum of a mean value and a fluctuating component, $\rho(r) = \bar{\rho} + \rho'(r)$. Since the mean component is the same for all values of r, the left-hand side of Eq. (12) is equivalent to the difference of fluctuations $\rho'(r - \frac{\Delta r}{2}) - \rho'(r + \frac{\Delta r}{2})$. Next, if

Δr is small with respect to the length scale of fluctuations, the spatial derivative of ρ' at some radial coordinate r_i can be approximated as

$$\frac{d\rho'(r_i)}{dr} \approx -\left(\frac{\rho'(r_i - \frac{\Delta r}{2}) - \rho'(r_i + \frac{\Delta r}{2})}{\Delta r}\right). \tag{14}$$

Finally, expanding the radial density fluctuation $\rho'(r)$ into a Taylor series at some radial coordinate r_i and neglecting higher-order terms,

$$\rho'(r) = \rho'(r_i) + \frac{d\rho'(r_i)}{dr}(r - r_i). \tag{15}$$

Without its higher-order terms, the accuracy of this expansion will quickly deteriorate as r becomes distant from r_i. Nonetheless, the FLDI measurements are capable of providing a very fine mesh of $d\rho'/dr$ values due to their high temporal resolution, and the distribution of r_i can be chosen accordingly. A reasonable estimate of $\rho'(r)$ can be obtained by using Eq. (15) sequentially, with each point $\rho'(r_i)$ defining its neighbor $\rho'(r_{i+1})$. Remembering that the density fluctuations are confined to the volume described by the blast wave radius at any given time, i.e., $\rho'(+\infty) = 0$, this is best done in the reverse direction, starting from the most outside point

$$\rho'(r_i) = \rho'(r_{i+1}) - \frac{d\rho'(r_i)}{dr}(r_{i+1} - r_i). \tag{16}$$

As seen in Sec. II A, blast wave data are commonly presented in the literature in terms of acoustic pressure amplitudes. As such, it will be more convenient to express the FLDI measurements as pressure fluctuations rather than density. For the small, isentropic disturbances analyzed here, density and pressure fluctuations are related through the local sound speed as

$$p' = \rho' c_0^2. \tag{17}$$

In summary, the complete set of simplifying hypotheses detailed in the preceding paragraphs is listed below:

(a) FLDI
  i. Divergence angle of the beams is neglected.
  ii. Finite differentiation approximates a spatial derivative.
(b) Flowfield
  i. Symmetric around a center point or axis.
  ii. Negligible density gradients outside the wave front radius at any instant.
  iii. The wave front travels with uniform velocity within the relevant probing time.
  iv. Isentropic within the relevant probing volume.

It is worth noting that the flowfield reconstruction methodology presented here and the numerical representation of the FLDI detailed in Sec. II B only share Eq. (4). That equation refers to a general physical principle of the behavior of light through a transparent medium of variable density. Therefore, the methods of computational FLDI simulation and flowfield reconstruction from FLDI data may be regarded as mutually independent.

III. METHODS

A. Experimental setup

The experimental arrangement employed in this work is the same as that used in Ref. 8. Information relevant to flowfield reconstruction and simulation is repeated here for clarity.

The FLDI system was designed to operate in the HEG shock tunnel.[35] The laser source is an Oxxius LCX-532S DPSS with a nominal wavelength of 532.3 nm. The corresponding Gladstone–Dale constant for this wavelength is $K = 0.227 \times 10^{-3}$ m^3/kg. The orthogonally polarized pair of beams is produced and later recombined using a pair of Sanderson prisms,[36] allowing different beam separation distances Δx to be produced. Four values of Δx are analyzed, namely 76, 120, 175, and 252 μm. The beams are approximately Gaussian with a maximum diameter of 45 mm at the field lenses, which are 3.8 m apart.

The photodetector is a Thorlabs DET36A2 of nominal bandwidth 25 MHz connected to an amplifier and recorder with a 50 Ω termination. The signal is recorded with DC-coupling and a sampling rate of 100 MHz. The conversion of the voltage produced by the photodetector into the FLDI phase difference is performed following Ref. 37. Prior to measurements, the undisturbed response of the FLDI is adjusted to the region of maximum sensitivity.

The probed flowfield is generated by the electric spark of an automotive spark plug with a 4 mm separation between its electrodes. The resulting weak blast wave propagates with approximately the ambient sound speed at distances larger than 20 mm from its origin, as analyzed in Ref. 8. The flowfield topology is shown in Fig. 3, with a series of superimposed schlieren images. In addition to the blast wave propagating radially, Fig. 3 also shows a secondary wave that propagates diagonally upward. This is a reflection of the main wave front off the structure of the spark generator and will be considered in Sec. IV.

A diagram of the experimental setup is shown in Fig. 4. The spark generator can be moved with respect to the fixed FLDI depicted in Figs. 4(a) and 4(b) along the axis of beam separation, such that measurements can be taken and analyzed at multiple distances from the source, represented as R in the frames of the figure. Measurements are taken at 23 positions with nominal distances between the source and probing volume of 3–50 mm. The spacing between the probing positions is smaller near the source, and position uncertainty is estimated at ±0.25 mm. A single spark is generated for each measurement, with the disturbances allowed to fully dissipate before the next one. Despite the careful adjustment

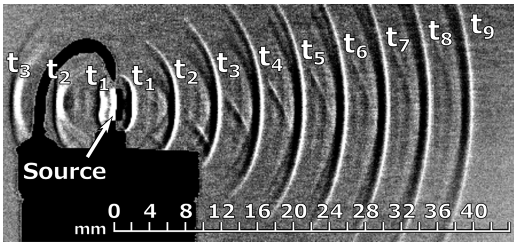

FIG. 3. Superposition of enhanced schlieren images of the blast wave generated using an automotive spark plug. The wave fronts at each instant in time are marked with the label t_i, with $t_i - t_{i-1}$ = 16.7 μs. Scale at the bottom in mm.

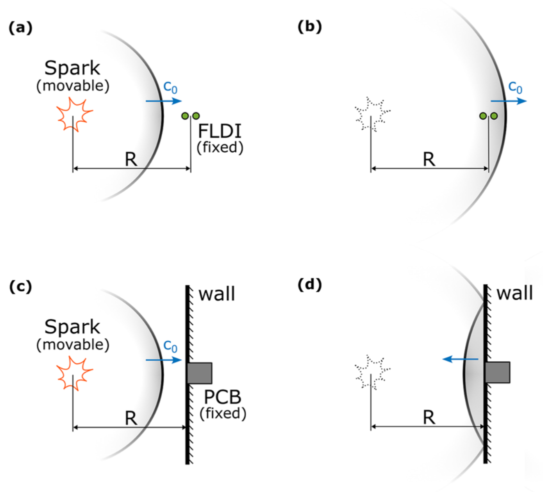

FIG. 4. Diagram of the experimental setup employed to acquire blast wave measurements. (a) and (b) Depict two moments of a given measurement with FLDI, before and after the blast wave reaches the probing location, respectively. (c) and (d) Depict the corresponding moments of a measurement using the wall-mounted PCB sensor. In (d), the blast wave front has reflected off the wall on which the PCB is mounted.

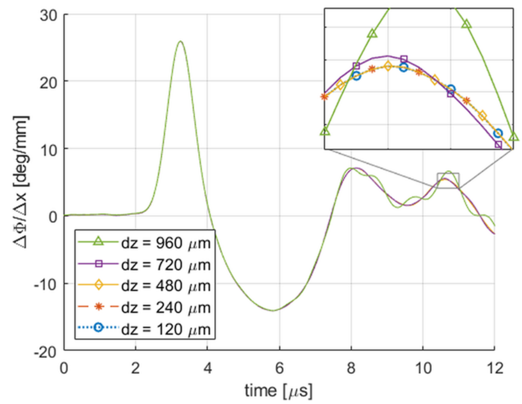

FIG. 5. Computational FLDI results of a blast wave using different mesh densities in the z direction. The mesh in z is defined by the uniform distance between two adjacent planes, denoted dz. Symbols are shown only in the detail inset for clarity.

and operation of the spark generator, eventual variations in flowfield generation have been observed during the tests. One possible reason is random changes in the spark breakdown path, which shift the origin and slightly alter the strength of the blast wave. Furthermore, although the experiments are conducted in a protected environment, it is not completely sealed, which may allow eventual small non-uniformities to be present in the surrounding medium. To minimize the effects of such eventual variations in flowfield generation, ten measurements are repeated at each position. The ambient sound speed is calculated using ambient temperature values obtained near the probing region before each series of measurements.

A separate series of blast wave measurements are conducted using a wall-mounted fast response piezoelectric pressure sensor PCB 132A32, as depicted in Figs. 4(c) and 4(d). The measurement approach is repeated from the FLDI measurements using the same movable spark generator setup. Starting at 16 mm from the source, the same nominal distances between the blast wave source and probing device are used. Measurements closer than this lower bound were hindered by geometric constraints. The pressure magnitudes obtained with the sensor are used as a reference for comparisons with the data post-processed from FLDI measurements. Due to the interaction between the flowfield and the wall, depicted in Fig. 4(d), a full waveform comparison is not possible. Nonetheless, the peak magnitude of overpressure detected at the wall upon reflection of the weak blast wave should be twice the overpressure of the incident wave.[29]

B. Computational FLDI

A mesh convergence analysis must be conducted before using the computational FLDI to perform flowfield evaluations. The discretization of the beam cross-section variables $\tilde{r}$ and θ follows a mutually dependent approach such that each mesh cell has an aspect ratio close to unity,[23] and z is discretized in uniform steps. A single waveform, based on experiments and representative of the data that will be detailed in Sec. IV C, is used to generate computational FLDI results with different meshes.

Figure 5 shows the simulation results for different discretization steps in z. The cFLDI solution is sensitive to this parameter in later moments of the simulation when the radial propagation of the disturbances causes a more varied distribution of field properties along the FLDI optical axis. Mesh-independent results for the discretization in z are obtained with a spacing of 480 μm and below. The value of 480 μm has been chosen for the subsequent evaluations.

Simulations were performed varying the number of divisions in the cross-section coordinate θ, shown in Fig. 6. Slight mesh-dependent variations are observed for the peak absolute values of the difference $\Delta\Phi$. These regions correspond to the largest flowfield gradient magnitudes, which require fine meshes to be sufficiently resolved. Since the radial discretization is linked to the steps in θ, the refinement of this parameter has a strong impact on the computational requirement of the simulation. Between 144 and 576 divisions in θ, the relative maximum difference in the simulated signal was only 0.5%. Therefore a number of 144 divisions were chosen as a balance between mesh convergence and computational cost. The corresponding number of divisions in the radial direction was 176.

The waveform used in this analysis corresponds to measurements obtained 30 mm away from the spark source, which is the location to be explored in detail in Sec. IV C. Due to the varying flow topology crossing the FLDI beams at each location, a similar mesh convergence study as presented here must be repeated accordingly if different locations are to be simulated.

IV. RESULTS AND DISCUSSION

A. Experimental data and processing

Figure 7 shows exemplary time-resolved experimental signals obtained at a number of probing locations and all four system configurations. The signals are minimally post-processed to yield phase

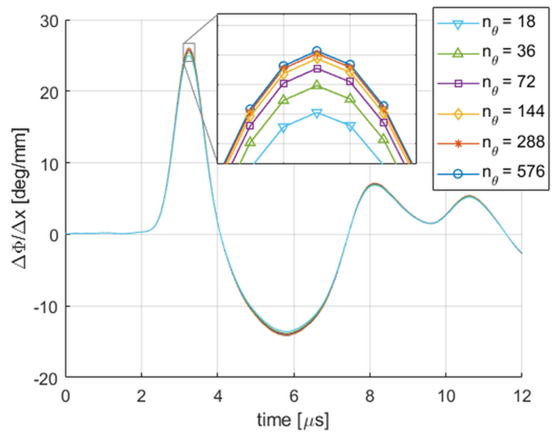

FIG. 6. Computational FLDI results of a blast wave using different beam cross-section meshes. The mesh in θ is defined by the number of divisions around the circumference n_θ, and the discretization in the radial direction is such that the aspect ratio of each cell remains close to 1. Symbols are shown only in the detail inset for clarity.

differences $\Delta\Phi$ and divided by the corresponding differentiation distance Δx to allow direct magnitude comparison.

The experimental signals from all probing locations were passed through a Savitzky–Golay filter for noise reduction and processed using the procedure detailed in Sec. II C to obtain pressure waveforms. The compression phase duration was noted to be the most sensitive parameter to non-uniformities in blast wave generation. Since the blast wave correlations presented in Sec. II A depend on the global behavior of the wave as it travels away from the source, for each measurement location, the waveforms with the highest and lowest values of compression phase duration were excluded as outliers. The remaining eight waveforms were combined into an average pressure profile, representative of the respective location, for further analysis.

Figure 8 shows the spatial evolution of pressure waveforms $p'(r)$ detected with the FLDI for all four system configurations. Note that the spatial waveforms in Fig. 8 travel from left to right, presenting a reversed profile along the x axis compared to the temporal traces in Fig. 7 [see Eq. (13)]. Each distinct line in Fig. 8 corresponds to the blast wave detection at a given location as the spark generator was consecutively moved away from the optical axis of the FLDI. The waveforms are spatially distributed such that they cross the respective measurement location with half their peak pressure. Where available, the reference peak pressures measured with the wall-mounted PCB pressure sensor are also shown, divided by a factor of two as mentioned in Sec. III A.

The typical blast wave profile with a sharp and strong compression front followed by a longer and less intense expansion region is observed in the vicinity of the spark generation. As the wave front propagates radially, the N-wave shape becomes evident, with approximately symmetric compression and expansion phases. The inset in Fig. 8 shows in detail the waveform obtained for R = 30 mm as an example. Small differences between the lines for each Δx can be seen, which will be further explored in Sec. IV C with aid from computational FLDI. The positive pressure seen at the trailing edge of the waveforms (e.g., near the left-hand edge of the inset) is a secondary wave that stems from the reflection of the main wave front on the structure of the spark generator. This is seen as an oblique trace propagating diagonally upward in the flow topology shown in Fig. 3. The remainder of the secondary wave is cut off from the waveforms in Fig. 8 for clarity.

Concerning the reference peak magnitudes obtained with the wall-mounted PCB, the pressure data reconstructed from FLDI measurements present an overall good agreement. Downstream of ~30 mm, a consistent small difference in peak magnitudes is apparent, with the PCB data always higher. This may be an effect of the trailing secondary wave mentioned earlier. Referring again to Fig. 3, this secondary wave front follows the main one closely along the center line in the vicinity of the 30 mm station. While the FLDI is still

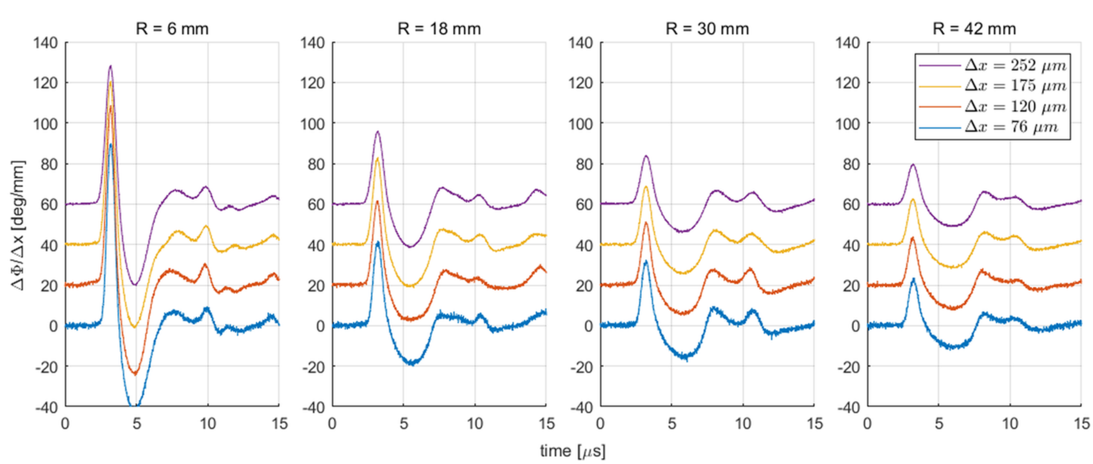

FIG. 7. Time signals obtained from FLDI measurements of spherical blast waves using multiple FLDI differentiation distances Δx, minimally post-processed. Each line is the average of ten overlapping time signals independently obtained at the same location and with the same Δx.

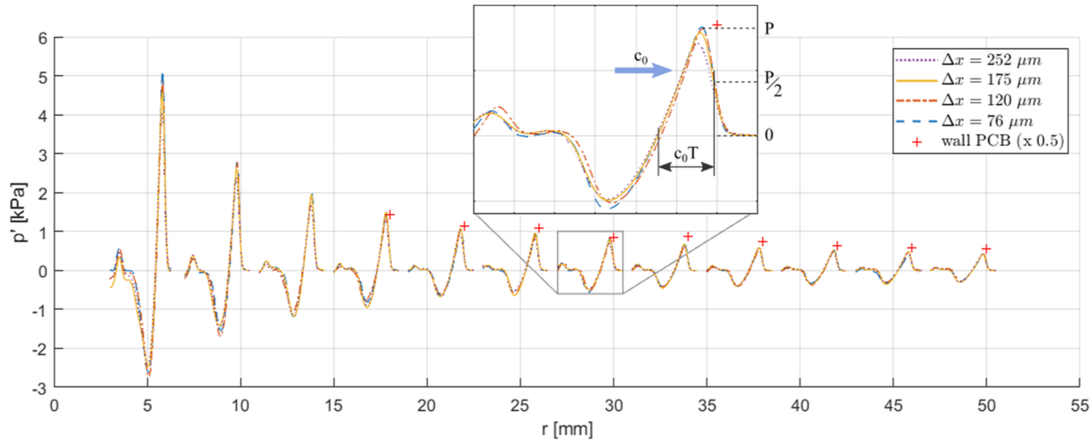

FIG. 8. Waveforms obtained from FLDI measurements of spherical blast waves using multiple FLDI differentiation distances Δx. The blast wave source is located at $r = 0$. Each profile is the average of eight waveforms independently obtained at the same location and with the same Δx. The displayed results are a subset of the complete dataset, selected for clarity such that consecutive waveforms do not overlap. The waveforms are aligned to their respective measurement location using half the peak pressure along the front of the wave. Corresponding reference peak pressures measured with a wall-mounted PCB pressure sensor are also shown where available.

capable of a clear detection of the main wave front, the interaction between the flowfield and the wall in the case of the pressure sensor favors the combination of the two waves, biasing the measured peak overpressures.

The physical analysis of the flowfield reconstructed from FLDI data can be continued by looking at the complete waveforms obtained. In addition to the peak pressure P, they also allow extracting the compression phase duration T, as illustrated in the inset of Fig. 8. To account for the finite thickness of the wave front, the value of half the peak pressure is used as a reference to obtain the compression phase duration as shown. The relationship between these two features, as expected from weak-shock theory, Eqs. (1) and (2), is analyzed next.

B. Analysis through weak-shock theory

The distributions of compression phase duration T from the reconstructed waveforms are shown in Fig. 9. Data for all analyzed Δx are shown, with an offset of one grid line between each adjacent dataset. Information obtained from the averaged pressure profiles is shown using empty symbols with dashed lines. The values obtained from each individually performed measurement are shown as filled small symbols on the background for completeness. The least-squares linear fits of T^2 vs $\log R$ for each case are shown as solid lines.

The sets of values from individual waveform regressions shown in Fig. 9 display an evident scatter toward the larger evaluated distances. This is attributed to a combination of two factors. First, small variations in the strength of the generated spark across the repetitions may yield pronounced accumulated differences as the wave propagates further away from the source. Second, as the amplitude of the detected signal becomes smaller, an eventual weak signal offset, either positive or negative, preceding the arrival of the wave front may bias the results of the integration procedure for waveform reconstruction, Eq. (12). The average of signal magnitude in a 10 μs range before the first signal rise is used to offset the zero level, in an attempt to avoid this. However, low signal-to-noise ratios reduced the accuracy of the offset in some cases. This is further evidenced by the fact that scatter is larger for smaller Δx values, in which case overall smaller signal amplitudes are produced. The biasing effect is small, as will be verified next with the fluctuation of peak pressures in this region. However, its influence on the evaluation of compression phase duration may be significant. A change in peak pressure will cause a proportional change in the compression phase duration (refer to the inset in Fig. 8). With the compression phase duration

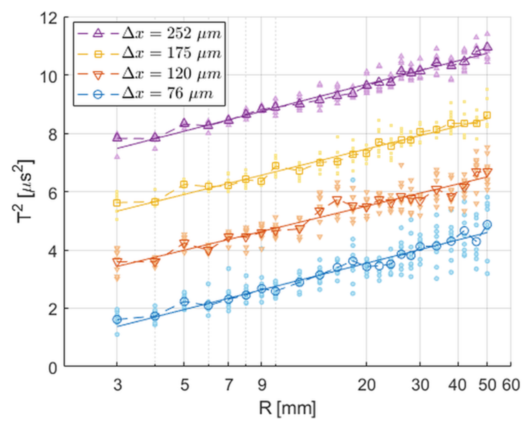

FIG. 9. Distribution of compression phase duration of spherical blast waves detected with FLDI using multiple differentiation distances Δx. Data are cascaded along the y axis with a positive offset of 2 μs^2 for each increasing Δx for clarity. Empty large symbols with dashed lines correspond to the mean waveforms, while filled small symbols in the background correspond to each independently regressed waveform. Linear fits for the distributions are shown as solid lines.

becoming ever larger as the wave propagates further, a small relative change in peak pressure may yield a noticeable change in the compression phase duration in terms of absolute values.

The observed scatter highlights the importance of performing repeated measurements across the probed distances. By considering the averaged waveform to obtain representative values for each location, the influence of the detailed factors is greatly reduced. This is verified by the generally low deviation between the data from averaged waveforms and a straight line, as expected from Eq. (1), and the similar slope independently obtained for each case.

Figure 10 shows the peak pressure data obtained for each case. Again, the datasets are cascaded for clarity, and values for the mean and individual waveforms are shown as empty symbols with dashed lines and filled small symbols, respectively. The comparatively low scatter of the values based on individual waveforms confirms that the non-uniformities mentioned earlier have a small effect on the peak pressures.

The complete dataset of reference peak pressures obtained with the wall-mounted PCB sensor is also shown, and repeated accordingly for each FLDI configuration. The logarithmic scale of Fig. 10 highlights the agreement between peak pressures measured with FLDI and the wall-mounted PCB for $R \leq 30$ mm. The PCB measurements beyond that location present a vertical offset. Nonetheless, they remain described by a straight line, as would be the case with a slightly stronger blast wave. This is evidence of the combination between the main and trailing wave fronts downstream of R = 30 mm, mentioned previously.

Proceeding with the analysis of the FLDI measurements, the slopes obtained from Fig. 9 are used to determine a σ_0 for each measured value of T (refer to Sec. II A) from the averaged waveforms. The corresponding values of peak pressure P expected from the weak-shock theory are then calculated for each measurement position using Eq. (2). The resulting distribution for each case is shown with a solid line in Fig. 10. For the waveforms reconstructed from FLDI measurements to be physically consistent, the solid and dashed lines in Fig. 10 must overlap.

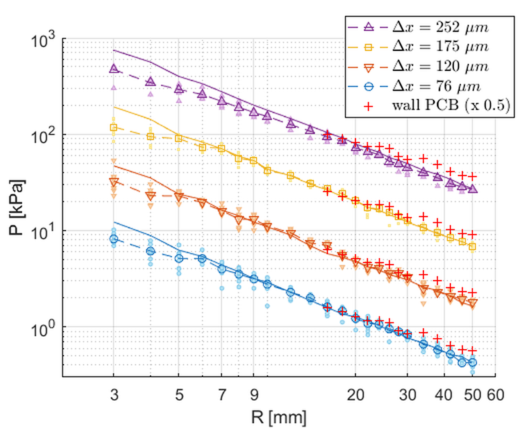

FIG. 10. Distribution of peak pressures of spherical blast waves, detected with the FLDI using multiple differentiation distances Δx. Data are cascaded along the y axis with a positive offset in factors of 4 for each increasing Δx for clarity. Empty large symbols with dashed lines correspond to the mean waveforms, while filled small symbols in the background correspond to each independently regressed waveform. The distributions of peak pressures expected from weak-shock theory based on mean T are shown as solid lines. Reference peak pressures measured with a wall-mounted PCB pressure sensor are also plotted where available.

A pronounced disagreement is noticed in the vicinity of the blast wave source for $R < 6$ mm. This may be due to a poor approximation of the blast wave as spherical in this region since the spark length is ~4 mm. In the case of a purely spherical blast wave, e.g., generated using laser induced breakdown as in Ref. 38, it could be expected that pressures in the close vicinity of the blast wave source would be higher,[39] rising to match the theoretical predictions. The predictions themselves would not be expected to change, given that the slopes in Fig. 9 are a global parameter and the compression phase durations shown in that same figure seem to follow a constant slope all the way through.

Away from the blast wave source, Fig. 10 shows an overall good agreement between measured and expected values for the three lower Δx values, in contrast to the consistent offset observed for $\Delta x = 252\ \mu$m. To quantify this offset, the point-wise ratios between the peak pressures measured on the FLDI waveforms P and the corresponding value expected from the weak-shock theory P_{ws} are calculated. The ratios for $R < 6$ mm are discarded for all cases for the reason mentioned earlier. Table I shows the mean and standard deviation values of P/P_{ws} observed for each case. For the three lower values of Δx, the distribution of P/P_{ws} is close to and varies across unity, indicating a reasonable match between the measured pressure peaks and the weak shock predictions. Conversely, for $\Delta x = 252\ \mu$m, a 10% offset is obtained on average, with the predicted values always greater than the measurements.

It is noted that only the separation distance Δx between the interferometric pair of the FLDI differentiates the four cases. These results indicate that the post-processing approach detailed in Sec. II C is able to yield physically consistent waveforms as long as the constraints imposed by the simplifications thereby listed are adequately considered. A value of $\Delta x = 252\ \mu$m likely violates simplification (a).ii, namely, the approximation of the finite difference performed by the FLDI to a spatial derivative. This is analyzed in further detail in Secs. IV C and IV D through cFLDI calculations.

C. Computational FLDI simulation

As seen in Sec. II C, the reconstruction of spherically propagating pressure waveforms using FLDI measurements is made possible through a series of approximations. In the following, the quality of the obtained waveforms is assessed by means of cFLDI to produce time-resolved phase difference $\Delta\Phi(t)$ simulations based on the reconstructed flowfield $p'(r)$. These computational results are

TABLE I. Compilation of ratios between peak pressures P measured from averaged waveforms and the corresponding values expected from the weak-shock theory P_{ws}, for each FLDI configuration. The mean and standard deviation values obtained from the distribution for $R \geq 6$ mm.

Δx	Mean P/P_{ws}
76 μm	0.992 ± 0.055
120 μm	1.033 ± 0.065
175 μm	1.009 ± 0.045
252 μm	0.894 ± 0.054

compared with the original experimental data. An accurate reconstruction must produce overlapping simulated results, meaning this cycle between measured or simulated $\Delta\Phi$ and reconstructed p' may go on indefinitely without any loss of information.

This approach is made possible by recalling that the methods of flowfield reconstruction and cFLDI simulation are entirely independent from each other, as seen in Sec. II. Since the ray-tracing cFLDI is physically accurate, a match between the simulation of a flowfield reconstructed from experiments and the experimental data that originated it implies that the reconstruction is also accurate (provided the possibility of non-unique solutions can be neglected). Any deviation between computed and experimental data is, therefore, an indication of flaws in the flowfield reconstruction procedure.

Figure 11 illustrates how the cFLDI perceives the passage of the blast wave. The wave front is marked with a darkened surface, and the FLDI beams are painted according to the instantaneous local density distribution. Due to the small time of interaction between the FLDI and the disturbance carried by the blast wave, the shape of the disturbance is assumed to be frozen in time and moving radially with a constant velocity. The temporal resolution for the computational FLDI calculations is chosen to be 20 MHz, based on a convergence analysis similar to the one presented for the mesh discretization in Sec. III B.

Careful evaluation of the reconstructed flowfield was conducted at $R = 30$ mm for all four Δx values. The observations presented next are specific to this probing location, but the methodology is general.

An averaged experimental time-resolved phase difference $\Delta\Phi$ was obtained for each differentiation distance Δx, and processed into a spatially resolved pressure flowfield to be simulated with cFLDI. The approach with averaged experimental data has the benefit of smoothing out eventual flowfield imperfections while keeping the signal main features. A clear reference is thus obtained to compare the computational results after completing the reconstruction–simulation cycle, improving the detection of eventual differences stemming from the reconstruction procedure.

Figure 12 shows the comparison between experimental and computed data. Results are displayed as the ratio between phase difference $\Delta\Phi$ and beam separation Δx. With such scaling, all lines are ideally identical regardless of FLDI configuration since the same disturbance field is probed at the same location across the cases. A vertical offset of 20°/mm is used between adjacent cases for clarity. The time origin in each case is arbitrarily defined such that the peak signals are aligned to facilitate visual comparison. The gray lines in the main plot show the original experimental data in each case, with colors denoting the cFLDI output of the corresponding reconstructed pressure waveforms.

The experimental signals across all four cases are verified to present a similar general form. All time series show the detection of the main wave front starting at ~2.5 μs and the previously mentioned secondary wave front close to 10 μs. The most noticeable difference is more apparent noise as Δx is smaller, which is a consequence of the overall lower signal amplitudes obtained with a small differentiation distance. The signals displayed as $\Delta\Phi/\Delta x$ represent a finite difference approximation of a spatial derivative. Considering the reduction of non-uniformities through averaging repeated measurements, the flowfield is essentially the same for all cases. Therefore, all experimental signals are ideally the same in terms of $\Delta\Phi/\Delta x$, as long as Δx is small enough. The experimental lines in Fig. 12 show this to be the case for $\Delta x = 76$ and 120 μm. For the higher Δx, a reduction in peak value and a damping of gradients are observed, especially for $\Delta x = 252$ μm. Those are indications that the finite difference operated by the FLDI is not performed across a small enough spatial interval to adequately represent a spatial derivative in this flowfield.

More insight can be gained from the cFLDI results. The colored lines in the main plot of Fig. 12 show that all four cases are mostly

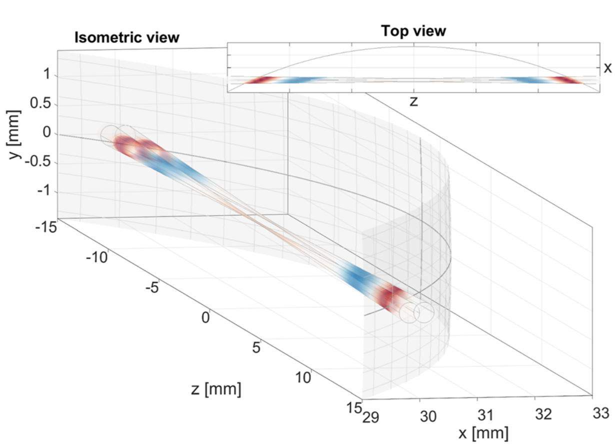

FIG. 11. Illustration of the computational FLDI of a blast wave, in isometric and top views. Colors are contours of density perturbation within the FLDI domain, with positive and negative variations indicated as tones of red and blue, respectively. The FLDI bundle is positioned 30 mm away from the blast wave source, with beams 252 μm apart in this example. At the moment of this snapshot, the blast wave radius is ~32.7 mm. The wave front is marked by a darkened surface.

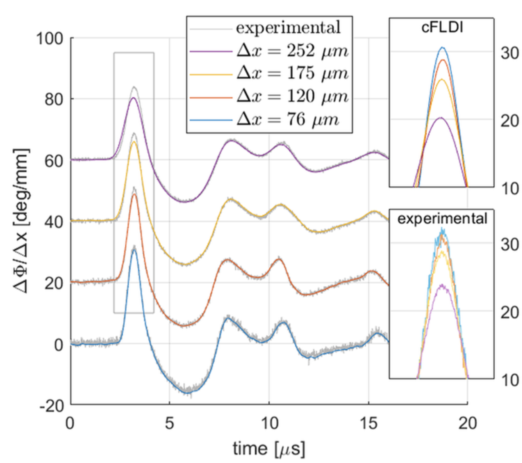

FIG. 12. Comparison of FLDI response to spherical blast waves, detected at 30 mm from the source using multiple FLDI differentiation distances Δx. Magnitudes are the ratio of phase difference to beam separation distance, offset in multiples of 20°/mm. Time origins are arbitrarily defined. The gray lines correspond to experimental measurements; colors represent the cFLDI response to the reconstructed disturbance field. The insets on the right refer to the box in the main plot with the vertical offsets removed, offering a direct comparison between the peak values of each experimental and cFLDI dataset.

well reproduced. The exceptions concern the sharp signal rise upon blast wave arrival. For Δx = 252 and 175 μm, a damping of gradient and reduction of peak value are again observed, more evidently for the former. This corroborates the previous observations concerning the experimental results. At this point, flowfield feature losses due to inadequate FLDI configuration have taken place twice: once when the experimental measurements were performed and again when the computational FLDI responses were simulated. The computational FLDI results in Fig. 12 also evidence small differences in peak values for Δx = 120 μm (and very small for Δx = 76 μm).

Table II evaluates these disagreements. For each Δx, the relative peak signal difference and the zero-lag cross-correlation between experimental and computational FLDI for the main wave front (between 1 and 10 μs in Fig. 12) are given. The cross-correlation is normalized by the auto-correlation of the experimental signal, such that both shape and amplitude differences result in a departure from unity. The listed values evidence the influence of Δx on the ability to return the reconstructed flowfield back into FLDI data. For the smallest evaluated Δx, good agreement is confirmed, with a loss in peak value of less than 3% and the overall time signal from the FLDI simulation correlating with the experimental one at 0.5%.

These observations allow the definition of two types of inaccuracies. First, on the ability of the FLDI as an instrument to detect strong gradients due to finite differentiation. Second, on the effect of simplifications adopted in Sec. II C to allow reconstruction of the blast wave flowfield from FLDI measurements. The former is seen in the raw experimental data as the signals present loss of features if Δx is above a certain threshold ($\Delta x > 120$ μm, in this case) and is unrelated to the post-processing methodology. The latter is verified when the physically accurate computational FLDI fails to reproduce the experimental signal from which the flowfield was obtained, therefore being of relevance in this work.

Interestingly, the cFLDI indicates a noticeable peak signal loss for Δx = 120 μm even though the experimental signal used to reconstruct the waveform was seemingly sufficiently resolved, as indicated by the nearly identical experimental $\Delta\Phi/\Delta x$ for Δx = 120 and 76 μm. Furthermore, it is noted that the differences observed in Fig. 12 and reported in Table II are mostly subtle for all cases other than Δx = 252 μm. It is evidenced that the comparison between measured and expected values of the reconstructed waveforms performed in Sec. IV B was only able to identify flaws for the highest Δx, despite the cFLDI results presenting discrepancies against the experimental data for other Δx values as well. This highlights the contribution of the cFLDI analysis to verify post-processing approaches, especially in the absence of parallel, reliable measurements to provide further support. These results are analyzed in more detail next, in view of the methodology proposed in Sec. II C and the list of simplifying hypotheses presented in its closing paragraph.

TABLE II. Quantitative comparison between experimental FLDI data and the cFLDI output to the reconstructed disturbance field. Values concern the spherical blast wave detected 30 mm from its source using multiple FLDI differentiation distances Δx. The peak signal difference is relative to the experimental signal, and the cross-correlation coefficient is normalized by the auto-correlation of the experimental signal.

Δx	Relative peak signal difference (%)	Normalized cross-correlation coefficient
76 μm	2.74	0.9950
120 μm	6.12	0.9849
175 μm	9.20	0.9704
252 μm	14.48	0.9556

D. Analysis of post-processing simplifications

It is first noted that agreement between experimental and computational results presented in Sec. IV C was obtained for at least one Δx while all other FLDI parameters remained unchanged. This indicates that simplifications such as neglecting the divergence of the beams and their finite volume, hypothesis (a).i, do not significantly interfere with the field reconstruction for a blast wave and FLDI setup with the dimensions presented here. An investigation of this hypothesis can be performed through the cFLDI simulation of a hypothetical instrument in which only one of the beams crosses the disturbance field, the other remaining unaffected as if it was a reference beam. In the case of this single beam FLDI, the output of Eq. (12) from Sec. II C is used directly in Eq. (17) without the steps concerning the conversion of density differences into density fluctuation magnitude. This is similar to the Mach–Zehnder interferometer simulation in Ref. 31, with the additional capability of having a full three-dimensional beam in the present cFLDI. By comparing the input flowfield with the flowfield reconstructed from this single beam instrument output, it is possible to assess the effects pertaining to beam divergence in an isolated manner. The comparison between an input flowfield and the reconstruction from a single beam FLDI simulation using different beam divergence angles is shown in Fig. 13. The acoustic pressure of the blast wave at R = 30 mm is used as the reference flowfield. The results confirm that the effect of beam divergence angle for the FLDI setup used in the experiments is negligible, while for much larger angles, it would become relevant. In the case reported here, the effect observed in Fig. 13 is caused by an interaction between the wave front and the

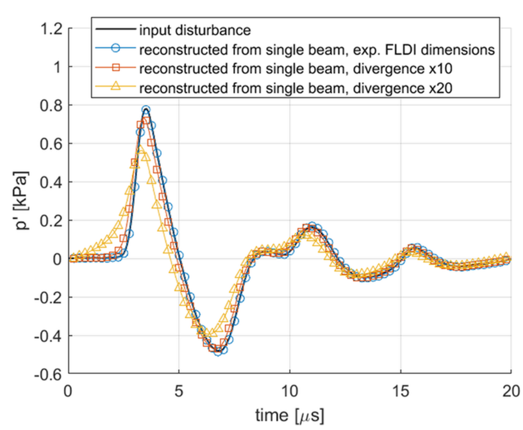

FIG. 13. Input blast wave acoustic pressure distribution in time, compared to reconstructed values from single beam computational FLDI simulations. Three different beam divergence angles are used in the simulations, namely, the divergence corresponding to the experimental setup in the present work (~0.7°), 10 times this value, and 20 times this value.

wide radius of the FLDI beams away from the focal plane before the blast wave reaches the FLDI focus.

Next, regarding the loss of accuracy as Δx becomes larger, an oversimplification regarding the finite beam separation, hypothesis (a).ii, is evidenced. This finite distance was disregarded when approximating the integral limits in Eq. (9) and the derivative in Eq. (14). These approximations can be analyzed separately as follows.

The approximation of the derivative through finite differences is a central hypothesis in the reconstruction method since the density value at each instant depends on the preceding value and the derivative following Eq. (16). An error in the finite difference approximation would misrepresent the local gradient, which in turn would introduce a local magnitude offset that would propagate to all subsequent points. In addition, recall that the flowfield reconstruction is performed spatially from outside the blast wave toward the inside. Hence, in the temporal simulated data in Fig. 12, the accumulated offset would become more significant at later times as the inner portions of the blast wave reach and travel through the FLDI location. Figure 12 shows that even for the largest Δx, the disagreement between experimental and computational results is limited to the first instants after blast wave arrival, with accurate reproduction later on. Therefore, the finite difference approximation is verified to be reasonable. This observation concerns the flowfield reconstruction method alone, even when the instrument itself might be ill-conditioned to perform the detection as mentioned for the larger values of Δx in the present case.

Conversely, the approximation of the integral limit can be particularly inaccurate in the brief moments following blast wave arrival. During this time interval, the disturbance field affects exclusively the upstream beam, and the combination of the integrals from Eq. (4) through the approximation described in Eq. (9) is not valid. A representative distribution of derivatives in this region is still obtained, but the precise conversion to radial quantities in Eq. (12) is affected. Evidently, the time interval in which this misrepresentation is observed (and hence its effect) increases with increasing beam separation Δx. Figure 12 shows that for the blast wave measurements presented here, the influence of the misrepresentation is negligible for $\Delta x = 76\ \mu$m, while for $\Delta x \geq 120\ \mu$m it is not.

A parametric study was conducted using the experimental data and the cFLDI to evaluate this effect. For every probing location and FLDI configuration, a pressure waveform was reconstructed from the experiment. By including multiple probing locations, waveforms of different characteristics are considered, as previously illustrated in Fig. 8. Each waveform was simulated in a cFLDI using several values of Δx, encompassing smaller, identical, and larger values than the experimental ones.

Figure 14 displays an overview of the observed results. On the y axis of the figure, the difference in the simulated FLDI peak value with respect to each experimental counterpart is represented as a percentage of loss. The abscissa shows the cFLDI differentiation distance Δx used in each simulation, normalized by the width of the compression front of the simulated waveform. Here, the width of the compression front refers to the first rising portion of the traveling pressure waveform, objectively defined as twice the distance between the waveform maximum pressure P and $P/2$ upstream of it, as annotated in the inset of Fig. 8. This normalization parameter is proposed to represent a region of strong gradients with a length across which

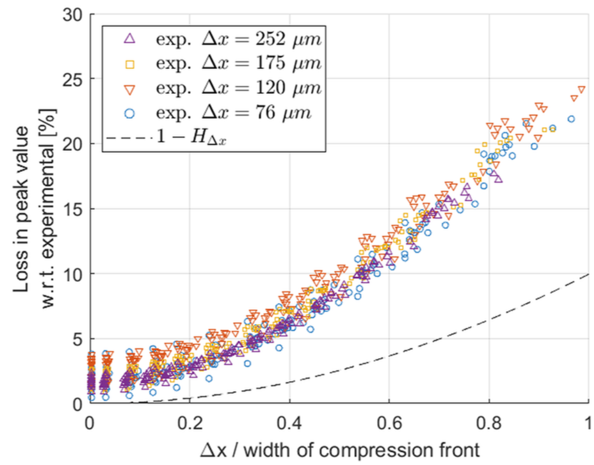

FIG. 14. Compilation of peak signal comparisons from parametric cFLDI analysis, performed over multiple probing locations and with different FLDI configurations. The y axis shows the percentage of loss on the peak of the cFLDI signal in terms of $\Delta\Phi/\Delta x$ with respect to the original experimental FLDI measurement used to obtain the computational flowfield. The x axis shows the value of FLDI differentiation distance Δx, normalized by the width of the compression front of each simulated pressure waveform. A reference value of expected loss due to finite differentiation is also given as $1 - H_{\Delta x}$, with $H_{\Delta x}$ being the transfer function corresponding to the finite difference.

the approximation of identical integral limits would not hold well. With the variation of FLDI differentiation distance reaching magnitudes comparable to a flowfield length scale, it becomes important to monitor losses caused by finite differentiation as well. This effect and that of the integral limit approximation overlap as functions of the differentiation distance and, therefore, cannot be analyzed separately. Nonetheless, an important distinction between these two effects is that the finite difference is physical, while the integral limit approximation pertains only to the flowfield reconstruction method. As such, the former is present in both experimental and computational FLDI, but the latter is exclusive to the cFLDI simulation. The transfer function describing the effect of finite differentiation distance as a function of wavenumber is given in Refs. 2 and 21 as $H_{\Delta x}(k) = \mathrm{sinc}(\Delta x \cdot k/2)$. The transfer function is used to calculate the loss in FLDI response magnitude expected for multiple values of $\Delta x \cdot k$, or $\Delta x \cdot 2\pi/\lambda$ in terms of disturbance wavelength, which is shown in Fig. 14. The width of the compression front used as the normalization parameter in the figure is assumed to be 1/4 of the wavelength of an equivalent sinusoidal disturbance.

It is first noted that for all cases, the loss in peak value is larger than the expected damping due to finite differentiation. This confirms that the approximation of the integral limit is the most constraining factor in the present flowfield reconstruction method. The results show a monotonic relationship between the cFLDI differentiation distance Δx and the ability of the simulated setup to reproduce the experimental signal, with lower values of Δx producing the best results. Furthermore, the width of the compression front of the probed waveform as a normalizing factor for Δx was able to approximately collapse this relationship, regardless of experimental FLDI configuration or probing location (the latter associated with different widths of the compression front, recall Fig. 8). The apparent larger spread of the points pertaining to the smaller experimental Δx is related to the lower signal-to-noise ratio in those cases, which introduces larger uncertainties in the determination of reference magnitudes. It is verified that for values of Δx less than 0.2 times the width of the flowfield compression front, the loss in the simulated value becomes a minimum, subject to other factors that may become dominant.

This general rule may be applied to the cases evaluated before, concerning the probing location of 30 mm away from the spark source, for verification. Using as a reference the experimental data obtained with $\Delta x = 76\ \mu$m, the obtained compression front width was ~0.32 mm. It is noted that $\Delta x = 76\ \mu$m is close to 0.2 times this value, whereas $\Delta x = 120$, 176, or 252 μm are much higher, with losses indicated by Fig. 14 that are compatible with the ones reported in Table II.

V. CONCLUSION

This work presented a new, analytic post-processing methodology to extract quantitative information from Focused Laser Differential Interferometry (FLDI) measurements of flowfields possessing circular symmetry. In the absence of complementary experimental data for complete direct comparisons, a physically accurate computational FLDI was employed as a tool to assess the accuracy of the approach. Constraining conditions were identified, and the methodology was confirmed to be reasonable if these conditions are met.

The methodology was applied and analyzed in FLDI measurements of spark-generated spherical weak blast waves, using multiple FLDI differentiation distances and probing locations. In a first verification effort, the reconstructed pressure waveforms agreed with predictions from weak-shock theory at distances larger than 6 mm from the spark source, below which the approximation of a spherical blast wave used by the theoretical model is not adequate. The agreement was observed for all but the largest differentiation distance, namely, $\Delta x = 252\ \mu$m, which showed consistently lower peak pressure values. Where allowed by experimental constraints, reference peak pressure values were obtained using a wall-mounted fast response piezoelectric pressure sensor. Comparisons between these references and the peak pressure magnitudes of the reconstructed waveforms provided similar observations.

An in-depth analysis of the reconstructed flowfield using cFLDI simulations helped identify further inaccuracies not captured in the theoretical comparisons, in terms of both peak signal amplitude and gradient damping. The simplification of equal integration lengths between the two beams composing the FLDI interferometric pair was identified as the most critical in the post-processing operations. Nonetheless, very good agreement was obtained between the computational FLDI for $\Delta x = 76\ \mu$m applied to the reconstructed flowfield and the experimental FLDI which gave origin to it. Differences were evaluated as less than 3% restricted to the close vicinity of the peak signal, and cross-correlation between the signals including all features agreed to 0.5%. The proposed post-processing methodology was hence verified to be sound, as long as a small enough Δx is employed. This threshold was evaluated by means of a parametric analysis using the cFLDI, as 20% or less of the length of the compression front, which represents a reference of strong spatial variation of density in the flowfield studied here.

It must be highlighted that the quantitative results presented in this work are specific to the blast wave flowfield investigated herein. Flowfields with different features or length scales might have different sensitivities to either Δx or other FLDI system properties. Nonetheless, the methodology of using cFLDI to evaluate such sensitivities can be extrapolated to different investigations. The approach detailed here is therefore recommended for any particular application, to ensure proper consideration of limiting constraints and obtain accurate post-processing output. The depth of insight offered by cFLDI as exemplified in this work is a strong argument for encouraging the widespread application of such simulations as an instrument of analysis.

ACKNOWLEDGMENTS

The support given by Professor Dr. Klaus Hannemann and Professor Dr. Peter J. Klar is deeply appreciated. The authors also wish to acknowledge the assistance of the HEG team, in particular Ingo Schwendtke, Uwe Frenzel, Fabian Glasewald, Jan Martinez Schramm, and Divek Surujhlal.

AUTHOR DECLARATIONS

Conflict of Interest

The authors have no conflicts to disclose.

Author Contributions

Giannino Ponchio Camillo: Methodology (lead); Writing – original draft (lead). **Alexander Wagner**: Supervision (lead); Writing – review & editing (lead).

DATA AVAILABILITY

The data that support the findings of this study are available from the corresponding author upon reasonable request.

REFERENCES

[1] N. Parziale, "Slender-body hypervelocity boundary-layer instability," Ph.D. thesis, California Institute of Technology, Pasadena, CA, 2013.

[2] M. R. Fulghum, "Turbulence measurements in high-speed wind tunnels using focusing laser differential interferometry," Ph.D. thesis, The Pennsylvania State University, PA, 2014.

[3] J. S. Jewell, N. J. Parziale, K.-L. Lam, B. J. Hagen, and R. L. Kimmel, "Disturbance and phase speed measurements for shock tubes and hypersonic boundary-layer instability," in *32nd AIAA Aerodynamic Measurement Technology and Ground Testing Conference* (American Institute of Aeronautics and Astronautics, 2016).

[4] A. Ceruzzi and C. P. Cadou, "Simultaneous velocity and density gradient measurements using two-point focused laser differential interferometry," in *AIAA Scitech 2019 Forum* (American Institute of Aeronautics and Astronautics, 2019).

[5] E. K. Benitez, J. S. Jewell, and S. P. Schneider, "Focused laser differential interferometry for hypersonic flow instability measurements with contoured tunnel windows," in *AIAA Scitech 2020 Forum* (American Institute of Aeronautics and Astronautics, 2020).

[6]B. F. Bathel, J. M. Weisberger, G. C. Herring, R. A. King, S. B. Jones, R. E. Kennedy, and S. J. Laurence, "Two-point, parallel-beam focused laser differential interferometry with a Nomarski prism," Appl. Opt. **59**, 244–252 (2020).
[7]M. Gragston, T. Price, K. Davenport, Z. Zhang, and J. D. Schmisseur, "Linear array focused-laser differential interferometry for single-shot multi-point flow disturbance measurements," Opt. Lett. **46**, 154–157 (2021).
[8]G. P. Camillo and A. Wagner, "A low-effort and inexpensive methodology to determine beam separation distance of multi-foci FLDI," Exp. Fluids **63**, 53 (2022).
[9]N. J. Parziale, J. E. Shepherd, and H. G. Hornung, "Observations of hypervelocity boundary-layer instability," J. Fluid Mech. **781**, 87–112 (2015).
[10]E. K. Benitez, S. Esquieu, J. S. Jewell, and S. P. Schneider, "Instability measurements on an axisymmetric separation bubble at Mach 6," in *AIAA AVIATION 2020 FORUM* (American Institute of Aeronautics and Astronautics, 2020).
[11]Y. Xiong, T. Yu, L. Lin, J. Zhao, and J. Wu, "Nonlinear instability characterization of hypersonic laminar boundary layer," AIAA J. **58**, 5254–5263 (2020).
[12]K. J. Hopkins, H. Porat, T. J. McIntyre, V. Wheatley, and A. Veeraragavan, "Measurements and analysis of hypersonic tripped boundary layer turbulence," Exp. Fluids **62**, 164 (2021).
[13]F. Siddiqui, M. Gragston, and R. D. W. Bowersox, "Measurement of wall-cooling effects on hypersonic boundary-layer transition using focused laser differential interferometry," AIAA J. **60**, 6214–6224 (2022).
[14]G. S. Settles and M. R. Fulghum, "The focusing laser differential interferometer, an instrument for localized turbulence measurements in refractive flows," J. Fluids Eng. **138**, 101402 (2016).
[15]B. Birch, D. Buttsworth, and F. Zander, "Measurements of freestream density fluctuations in a hypersonic wind tunnel," Exp. Fluids **61**, 158 (2020).
[16]A. Hameed and N. J. Parziale, "Focused laser differential interferometry transfer functions for complex density disturbance fields," in *AIAA AVIATION 2021 FORUM* (American Institute of Aeronautics and Astronautics, 2021).
[17]A. Hameed and N. J. Parziale, "Focused laser differential interferometric investigation of turbulent jet spectra," J. Spacecr. Rockets **59**, 1565–1573 (2022).
[18]A. P. Ceruzzi and C. P. Cadou, "Interpreting single-point and two-point focused laser differential interferometry in a turbulent jet," Exp. Fluids **63**, 112 (2022).
[19]A. P. Ceruzzi, "Development of two-point focused laser differential interferometry for applications in high-speed wind tunnels," Ph.D. thesis, University of Maryland, College Park, MD, 2022.
[20]A. Ceruzzi, C. Neisess, B. McManamen, and C. P. Cadou, "Investigation of focused laser differential interferometry (FLDI) sensitivity function," in *AIAA Scitech 2021 Forum* (American Institute of Aeronautics and Astronautics, 2021).
[21]J. M. Lawson, "Focused laser differential interferometry," Ph.D. thesis, California Institute of Technology, Pasadena, CA, 2021.
[22]J. M. Lawson, M. C. Neet, J. W. Hofferth, and J. M. Austin, "Supersonic freestream density fluctuations from focused laser differential interferometry and pitot-probe measurements," AIAA J. **60**, 5173–5186 (2022).
[23]B. E. Schmidt and J. E. Shepherd, "Analysis of focused laser differential interferometry," Appl. Opt. **54**, 8459–8472 (2015).
[24]J. M. Lawson, M. C. Neet, I. J. Grossman, and J. M. Austin, "Static and dynamic characterization of a focused laser differential interferometer," Exp. Fluids **61**, 187 (2020).
[25]J. M. Lawson and J. M. Austin, "Focused laser differential interferometer response to shock waves," Meas. Sci. Technol. **32**, 055203 (2021).
[26]E. K. Benitez, M. P. Borg, C. Rhodes, and J. S. Jewell, "Optical-axis spatial sensitivity of a simulated focused laser differential interferometer," AIAA J. 1–14 (2023).
[27]E. K. Benitez and J. S. Jewell, "Simulated focused laser differential interferometry of time-varying signals," in *AIAA SCITECH 2022 Forum* (American Institute of Aeronautics and Astronautics, 2022).
[28]E. K. Benitez, M. P. Borg, J. Luke Hill, M. T. Aultman, L. Duan, C. L. Running, and J. S. Jewell, "Quantitative focused laser differential interferometry with hypersonic turbulent boundary layers," Appl. Opt. **61**, 9203–9216 (2022).
[29]G. F. Kinney and K. J. Graham, *Explosive Shocks in Air*, 2nd ed. (Springer Berlin Heidelberg, New York, 1985).
[30]A. D. Pierce, *Acoustics*, 3rd ed. (Springer International Publishing, Switzerland, 2019).
[31]P. Yuldashev, M. Karzova, V. Khokhlova, S. Ollivier, and P. Blanc-Benon, "Mach-Zehnder interferometry method for acoustic shock wave measurements in air and broadband calibration of microphones," J. Acous. Soc. Am. **137**, 3314–3324 (2015).
[32]W. M. Wright, "Propagation in air of *N* waves produced by sparks," J. Acous. Soc. Am. **73**, 1948–1955 (1983).
[33]M. Born and E. Wolf, *Principles of Optics*, 7th ed. (Cambridge University Press, Cambridge, UK, 1999).
[34]M. M. Karzova, P. V. Yuldashev, V. A. Khokhlova, S. Ollivier, E. Salze, and P. Blanc-Benon, "Characterization of spark-generated *N*-waves in air using an optical schlieren method," J. Acous. Soc. Am. **137**, 3244–3252 (2015).
[35]Deutsches Zentrum für Luft - und Raumfahrt (DLR), "The High Enthalpy Shock Tunnel Göttingen of the German Aerospace Center (DLR)," J. Large-Scale Res. Facil. **4**, A133 (2018).
[36]S. R. Sanderson, "Simple, adjustable beam splitting element for differential interferometers based on photoelastic birefringence of a prismatic bar," Rev. Sci. Instrum. **76**, 113703 (2005).
[37]J. M. Lawson, M. C. Neet, I. J. Grossman, and J. M. Austin, "Characterization of a focused laser differential interferometer," in *AIAA Scitech 2019 Forum* (American Institute of Aeronautics and Astronautics, 2019).
[38]B. F. Bathel, J. M. Weisberger, G. C. Herring, R. Jagannathan, C. T. Johansen, S. B. Jones, and A. A. Cavone, "Analysis of the amplitude response of a two-point and a multi-point focused laser differential interferometer," in *AIAA Scitech 2021 Forum* (American Institute of Aeronautics and Astronautics, 2021).
[39]G. G. Bach and J. H. S. Lee, "An analytical solution for blast waves," AIAA J. **8**, 271–275 (1970).